

## Exciton Coupling in Redox-Active Salen based Self-Assembled Metallacycles

Dr. Khristyna Herasymchuk,<sup>a</sup> Dr. Magali Allain,<sup>b</sup> Gregory A. MacNeil,<sup>a</sup> Prof. Vincent Carré,<sup>c</sup> Prof. Frédéric Aubriet,<sup>c</sup> Prof. Daniel B. Leznoff,<sup>a</sup> Prof. Marc Sallé,<sup>\*b</sup> Dr. Sébastien Goeb,<sup>\*b</sup> and Prof. Tim Storr<sup>\*a</sup>

<sup>a</sup>Department of Chemistry, Simon Fraser University, Burnaby, Canada. E-mail:

[tim\\_storr@sfu.ca](mailto:tim_storr@sfu.ca); @storr\_tim

<sup>b</sup>Univ Angers, CNRS, MOLTECH-ANJOU, 2 bd Lavoisier, F-49000 Angers, France. E-mails: [sebastien.goeb@univ-angers.fr](mailto:sebastien.goeb@univ-angers.fr); [marc.salle@univ-angers.fr](mailto:marc.salle@univ-angers.fr);

<sup>c</sup>LCP-A2MC, FR 3624, Université de Lorraine, ICPM, 1 Bd Arago, 57078 Metz Cedex 03, France

### Abstract

The incorporation of a redox-active nickel salen complex into supramolecular structures was explored via coordination-driven self-assembly with homobimetallic ruthenium complexes (bridged by oxalato or 5,8-dihydroxy-1,4-naphthoquinato ligands). The self-assembly resulted in the formation of a discrete rectangle using the oxalato complex and either a rectangle or a catenane employing the larger naphthoquinonato complex. The formation of the interlocked self-assembly was determined to be solvent and concentration dependent. The electronic structure and stability of the oxidized metallacycles was probed using electrochemical experiments, UV-Vis-NIR absorption, EPR spectroscopy and DFT calculations, confirming ligand radical formation. Exciton coupling of the intense near-infrared (NIR) ligand intervalence charge transfer (IVCT) bands provided further confirmation of the geometric and electronic structures in solution.

### Introduction

Coordination controlled self-assembly of two-dimensional and three-dimensional structures has become one of the leading research areas in the field of supramolecular chemistry.<sup>[1,2,3,4,5,6,7,8,9,10]</sup> They are generally constructed from a metal complex and a ligand (or metalloligand) that can self-assemble into structural arrangements of diverse geometry and magnitude.<sup>[7,11,12,13,14,15,16,17,18,19,20,21]</sup> The energetic intermediacy of coordination bonds

(compared to covalent and weak non-covalent bonds) allows for reversibility and modulation of the self-assembly kinetics through the rigidity of the acceptors and donors to achieve a thermodynamic minimum.<sup>[2,22]</sup> Over the last two decades, interlocked systems, in particular catenanes,<sup>[23,24]</sup> rotaxanes,<sup>[23,25,26]</sup> Solomon links,<sup>[27,28,29,30,31,32]</sup> knots,<sup>[12,33,34]</sup> and Borromean rings<sup>[7,15,32,35,36,37,38]</sup> have received significant attention due to their intriguing structural arrangement and potential application as molecular machines and smart materials.<sup>[39,40]</sup>

A large number of these structures are constructed from arene-linked Ru, Rh and Ir metallacycles. In particular, homobimetallic ( $\eta^6$ -arene)ruthenium complexes for which two coordinating sites are parallel and bridged by O,O-chelating oxalato, 2,5-dihydroxy-1,4-benzoquinato, 5,8-dihydroxy-1,4-naphthoquinato, and 6,11-dihydroxy-5,12-tetracenedionato ligands, have been studied in depth by the groups of Therrien,<sup>[41,42,43,44,45]</sup> Chi,<sup>[33,46,47,48,49,50,51]</sup> Stang<sup>[52,53,54]</sup> and Jin<sup>[15,24,40,55]</sup> for example. Their easily tunable Metal–Metal distance makes these complexes ideal candidates for template-driven self-assembly of interlocked structures.<sup>[31,46,52,56]</sup>

In addition to having potential applications as smart materials, nanoscale devices, and molecular machines,<sup>[7]</sup> interlocked metallacyclic assemblies can display photophysical properties that may find applications in display technologies and photovoltaics.<sup>[57]</sup> Specifically, near-infrared (NIR) absorbing materials have optical and electronic applications<sup>[57]</sup> that have even been used in biomedical research.<sup>[58]</sup> Utilizing salen-type ligands (salen = N<sub>2</sub>O<sub>2</sub> *bis*(Schiff-base)-*bis*(phenolate)) in the supramolecular self-assemblies introduces mixed-valence species upon oxidation that can exhibit low energy ligand radical intervalence charge transfer (IVCT) bands in the NIR.<sup>[59,60,61,62,63]</sup> Metal complexes with redox-active ligands as part of the supramolecular assemblies and frameworks provide an opportunity for reactivity tuning and development of materials applications.<sup>[64,65,66,67,68,69]</sup>

Over five decades ago, Kasha described the relationship between molecular packing and photophysical properties in terms of spectral shifts, which are based on the alignment of transition moment dipoles and exciton coupling.<sup>[70,71]</sup> For instance, an in phase transition moment dipole alignment in a cofacial manner results in a blue-shifted absorption with doubled intensity in comparison to the monomer (Figure 1a). However, when this alignment is not planar, the interaction is evaluated based on the angle between

these transition moment dipoles (Figure 1b). Hence, the exciton model is useful in describing the resonance interaction between weakly coupled excited states. Our group has recently reported on a series of dimers with different orientations of the oxidized Ni salen ligand radical chromophores.<sup>[59,63]</sup> For example, a cofacial alignment in a Ni salen dimer showing a Ni...Ni distance of 3.98 Å in the neutral form results in a blue-shifted IVCT band of double intensity upon oxidation with respect to the oxidized monomeric analogue.<sup>[59]</sup> However, a Pd macrocycle containing four Ni salen units arranged into a square showed no exciton effect upon oxidation, due to the extended distance and 90° angle between the salen units.<sup>[72]</sup>

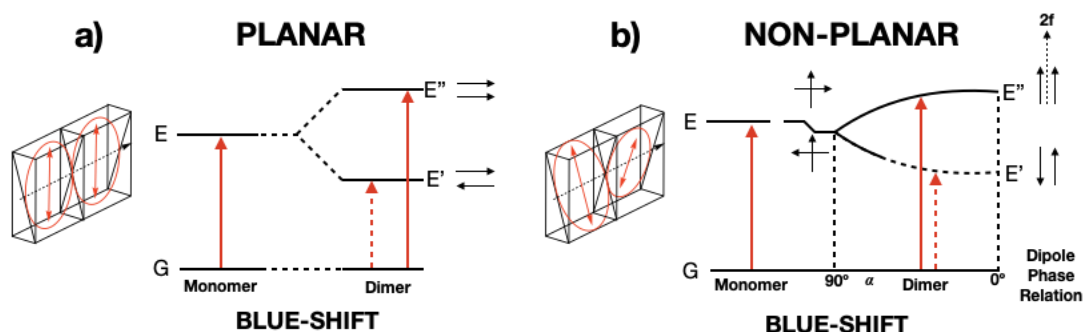


**Figure 1.** a) Planar and b) non-planar exciton models exhibiting band shifting and splitting for excited states in a planar orientation to one another (black arrows represent transition moment dipoles;<sup>[70,71]</sup> solid and dashed red arrows represent allowed and forbidden transitions, respectively).

Aside from our recent report on the coordination-driven self-assembly of the metallacycle containing Ni(Salen)<sup>pPy</sup> as a linker,<sup>[72]</sup> and characterization of its redox properties, the use of salen complexes in self-assembly is limited,<sup>[73,74,75]</sup> and the redox chemistry of the assembled macrocycles is virtually unexplored.<sup>[72]</sup> In this work, we outline the coordination-driven self-assembly of the redox-active metalloligand, Ni(Salen)<sup>pPy</sup> (**1**) with two bimetallic Ru complexes, *bis*-Ru(ox) (**2a**) and *bis*-Ru(naphtho) (**2b**) (Scheme 1). The two Ru complexes were chosen based on their Ru–Ru distances (5.5 Å vs. 8.3 Å), allowing for the self-assembly of these metallacycles to result in arrangements with varying salen-salen distances. Each assembly was characterized in the solid state and solution, and depending on the conditions, an interlocked assembly was determined to form when utilizing the larger *bis*-Ru(naphtho) acceptor. Macrocycle oxidation resulted in salen ligand radical formation with shifts in the associated near-infrared (NIR) intervalence charge transfer (IVCT) bands in comparison to the monomer analogue consistent with exciton coupling and maintenance of the macrocyclic structure in solution upon oxidation.

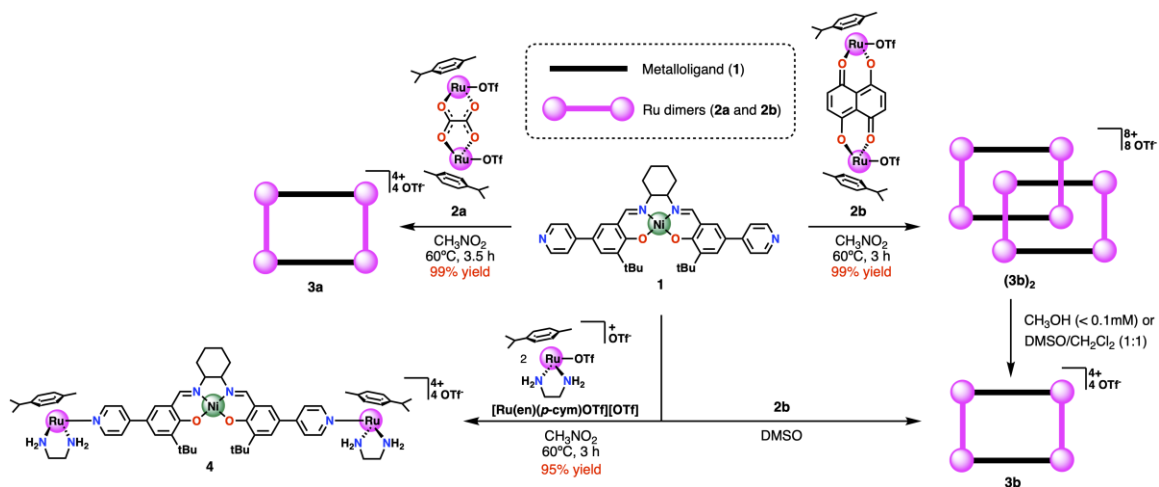
## Results and Discussion

### Synthesis and Characterization

The preparation of the linear ditopic metalloligand Ni(Salen)<sup>pPy</sup> (**1**) has been previously reported,<sup>[72]</sup> and the homobimetallic Ru pillars, **2a** and **2b** were synthesized according to previously described reports (See SI).<sup>[76,77]</sup> The assembly of metallacycles (**3a** and (**3b**)<sub>2</sub>) was achieved by reacting equimolar amounts of the ditopic metalloligand (**1**) and a ditopic pillar (**2a** or **2b**) in nitromethane at 60°C (C = 4.0 mM and 2.0 mM, respectively), as outlined in Scheme 1 (See Supporting Information for synthesis details). Conversion from (**3b**)<sub>2</sub> to **3b** can be achieved through the dilution of a methanol solution (< 0.1 mM) or solubilizing (**3b**)<sub>2</sub> in dimethyl sulfoxide/dichloromethane (1:1) solvent mixture (*vide infra*). Alternatively, **3b** can be produced from a dimethyl sulfoxide solution.

The synthesis and isolation of monomeric analogue **4** (Scheme 1) was necessary to better characterize and compare the redox properties of **1** to its macrocyclic counterparts as we have previously reported that oxidation of **1** results in intermolecular interaction of the terminal pyridyl groups with the Lewis acidic Ni centre.<sup>[72]</sup> The [Ru(en)(*p*-cym)OTf][OTf] (*p*-cym = *p*-cymene) complex was used as a node to cap the coordinating pyridyl moieties, and was synthesized in two steps (See SI).<sup>[76,78,79]</sup>

**Scheme 1.** Self-assembly of metallacycles **3a**, **(3b)<sub>2</sub>** and **3b** and monomer analogue **4**.



The self-assembly of **3a** and **(3b)<sub>2</sub>** was confirmed via Electrospray Ionization – Fourier Transform Ion Cyclotron Resonance (ESI-FTICR) mass spectrometry to unambiguously support the formation of the monomeric ( $\text{M}_2\text{L}_2$ , where  $\text{M} = \mathbf{2a}$  and  $\text{L} = \mathbf{1}$ ) self-assembly **3a** and a dimeric or interlocked ( $\text{M}_4\text{L}_4$ , where  $\text{M} = \mathbf{2b}$  and  $\text{L} = \mathbf{1}$ ) self-assembly **(3b)<sub>2</sub>**. Characteristic multicharged peaks for **3a** at  $m/z = 602.14$ ,  $852.49$ , and  $1353.20$ , correspond to  $[\mathbf{3a}-4(\text{OTf})]^{4+}$ ,  $[\mathbf{3a}-3(\text{OTf})]^{3+}$ ,  $[\mathbf{3a}-2(\text{OTf})]^{2+}$ , respectively (Figure S1). Similarly, multicharged peaks for **(3b)<sub>2</sub>** at  $m/z = 1132.82$ ,  $1453.25$  and  $1987.37$  correspond to  $[(\mathbf{3b})_2-5(\text{OTf})]^{5+}$ ,  $[(\mathbf{3b})_2-4(\text{OTf})]^{4+}$ , and  $[(\mathbf{3b})_2-3(\text{OTf})]^{3+}$ , respectively (Figure S2). The peaks at  $m/z = 652.16$ ,  $919.18$ , and  $1453.25$  are attributed to the presence of **3b** as  $[\mathbf{3b}-4(\text{OTf})]^{4+}$ ,  $[\mathbf{3b}-3(\text{OTf})]^{3+}$ , and  $[\mathbf{3b}-2(\text{OTf})]^{2+}$ , respectively, highlighting the lability of interlocked **(3b)<sub>2</sub>** in the gas phase.

Single crystals of **3a** and **(3b)<sub>2</sub>** were obtained from slow diffusion of diisopropyl ether (**3a**) or diethyl ether (**(3b)<sub>2</sub>**) into a concentrated solution in methanol/nitromethane (1:1) at room temperature. The solid-state structure of the metallacycle **3a** (Figure 2a, Tables S1-S2), confirms the  $\text{M}_2\text{L}_2$  assembly. The Ni salen units are staggered, with a  $\text{Ni}\cdots\text{Ni}$  distance of  $3.84 \text{ \AA}$ . The  $\text{Ni}\cdots\text{Ni}$  separation in **3a** is significantly shorter in comparison to the  $5.48 \text{ \AA}$  distance between the Ru centers in the pillar, and could be due to a crystal packing effect, and/or  $\pi$ - $\pi$  stacking of the salen units.<sup>[7,80]</sup> The crystal structure of metallacycle **(3b)<sub>2</sub>** (Figure 2b, Table S1) further supports that two  $\text{M}_2\text{L}_2$  assemblies are interlocked to form a [2]catenane as  $\text{M}_4\text{L}_4$ . Each Ni salen unit is separated by  $\sim 4.4\text{--}4.9 \text{ \AA}$  with a twist of  $\text{ca. } 50^\circ$  between each  $\text{M}_2\text{L}_2$  assembly (Figure 2b). Ni salen units belonging to each individual  $\text{M}_2\text{L}_2$  assembly are stacked (i.e., *t*Bu groups oriented in the same

direction), in contrast to **3a**. This orientation aids in minimizing steric interactions in the [2]catenane, as each adjacent salen unit is staggered, with an alternate orientation of <sup>t</sup>Bu groups. In both solid-state structures, the coordination sphere at the Ni centre closely resembles that of the **Ni(Salen)<sup>pPy</sup>** complex (**1**)<sup>[72]</sup> with a slightly distorted square planar geometry at the metal centre.

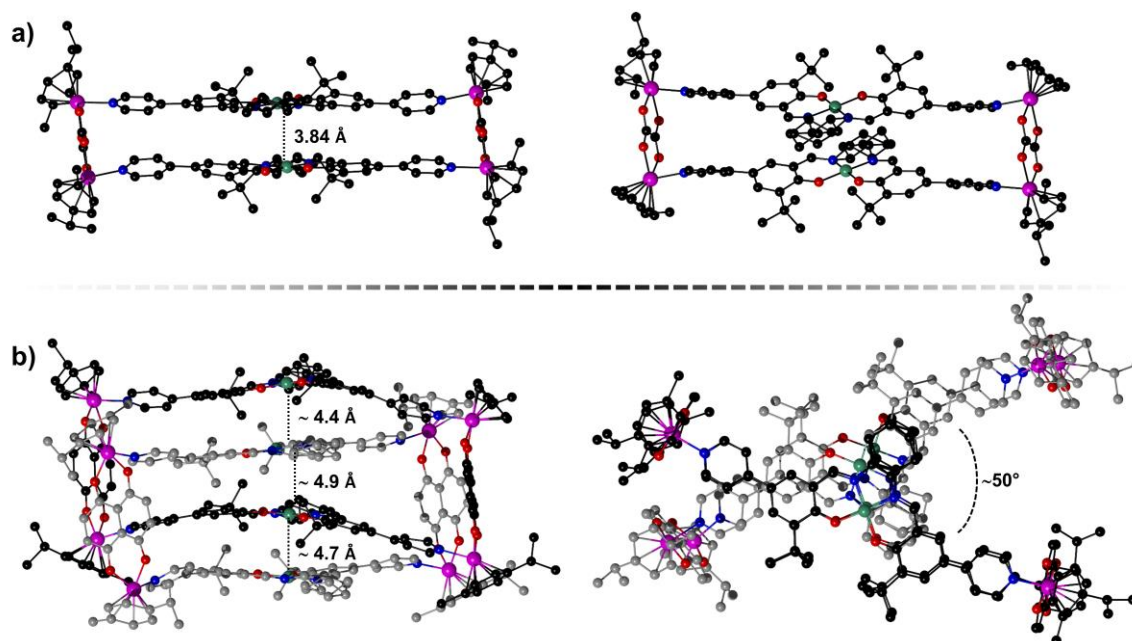


**Figure 2.** X-Ray crystal structures of metallaring **3a** (a) and interlocked structure **(3b)<sub>2</sub>** (b). Hydrogen atoms and counterions are excluded for clarity.

The initial self-assembly of the metallacycles in solution was monitored by <sup>1</sup>H NMR spectroscopy. The synthesis of **3a** and **(3b)<sub>2</sub>** was achieved in CH<sub>3</sub>NO<sub>2</sub> (at 4.0 and 2.0 mM, respectively) through pyridyl group coordination of **1** to the Ru(II) centres of the pillars **2a** and **2b**, respectively. <sup>1</sup>H NMR spectra of **3a** in CD<sub>3</sub>NO<sub>2</sub> (Figure 3a, S5 and S6) confirm a M<sub>2</sub>L<sub>2</sub>-type assembly and the formation of the rectangular metallacycle. An upfield shift of the α-pyridinyl and β-pyridinyl protons from 8.52 and 7.58 ppm in **1** to 7.87 and 7.44 ppm in **3a**, respectively, is due to the increased shielding from the adjacent π-electron-rich Ni salen unit.<sup>[31,81]</sup> The characteristic set of doublets for the *p*-cymene moiety were observed at 5.69 and 5.86 ppm in **3a**, shifted downfield slightly compared to **2a** (5.69 and 5.81 ppm).<sup>[31]</sup> To confirm a discrete assembly of the metallacycle and estimate its hydrodynamic

radius,  $R_h$ , Diffusion-Oriented Spectroscopy (DOSY) was used.  $^1\text{H}$  DOSY NMR of **3a** in nitromethane (Figure 3a) shows a single alignment of signals with a diffusion rate of  $D_{\text{NMR}} = 3.50 \times 10^{-10} \text{ m}^2 \text{ s}^{-1}$  in comparison to **1** ( $D_{\text{NMR}} = 1.38 \times 10^{-9} \text{ m}^2 \text{ s}^{-1}$ )<sup>[72]</sup>, confirming that only one discrete self-assembled structure exists in solution. Using the diffusion coefficient determined in the  $^1\text{H}$  DOSY NMR experiment and the Stokes-Einstein equation<sup>[82]</sup> the hydrodynamic radius for **3a** was calculated to be 10.4 Å in nitromethane (see Table S3 and description for the calculated value).

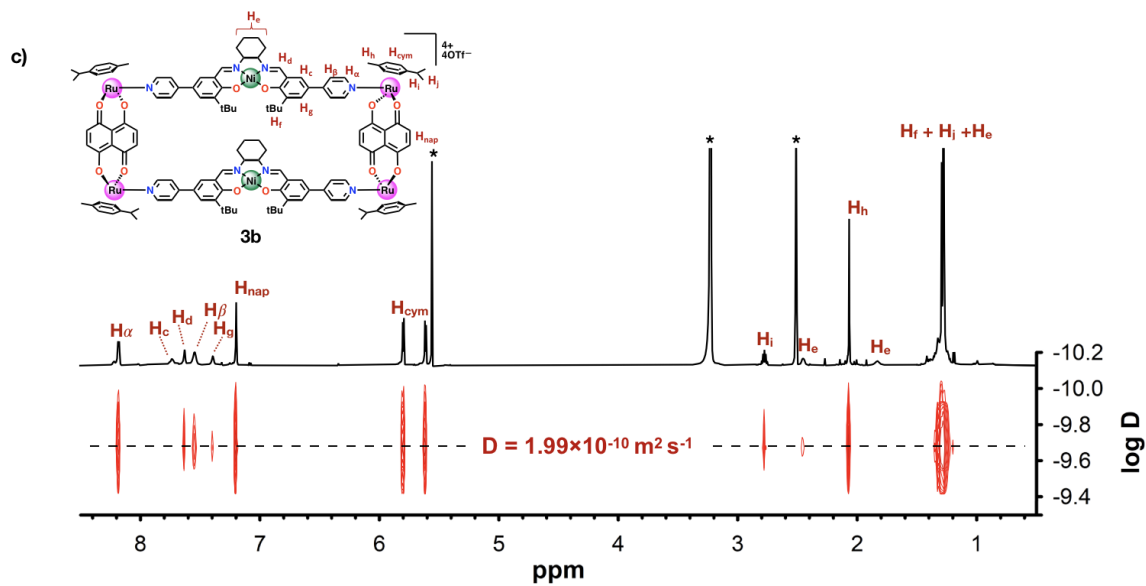
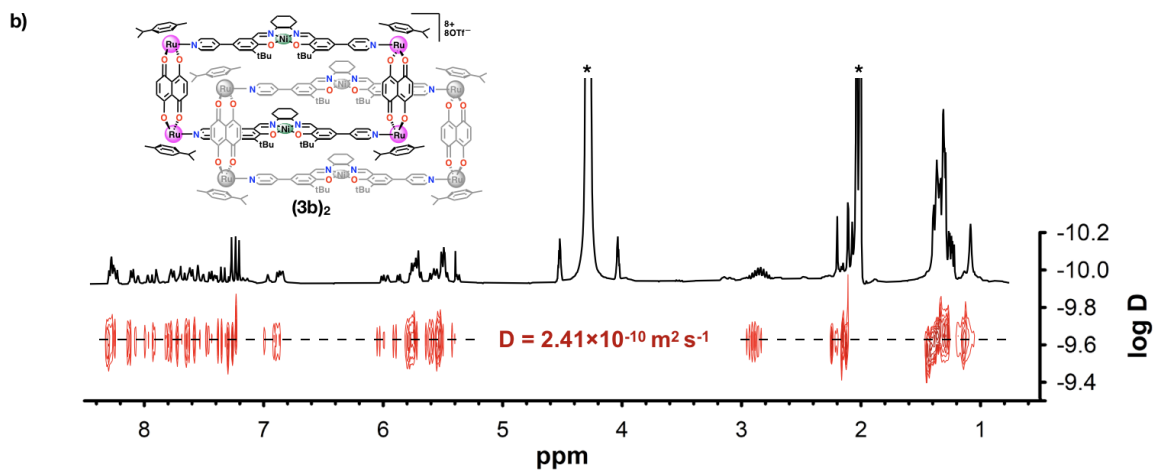
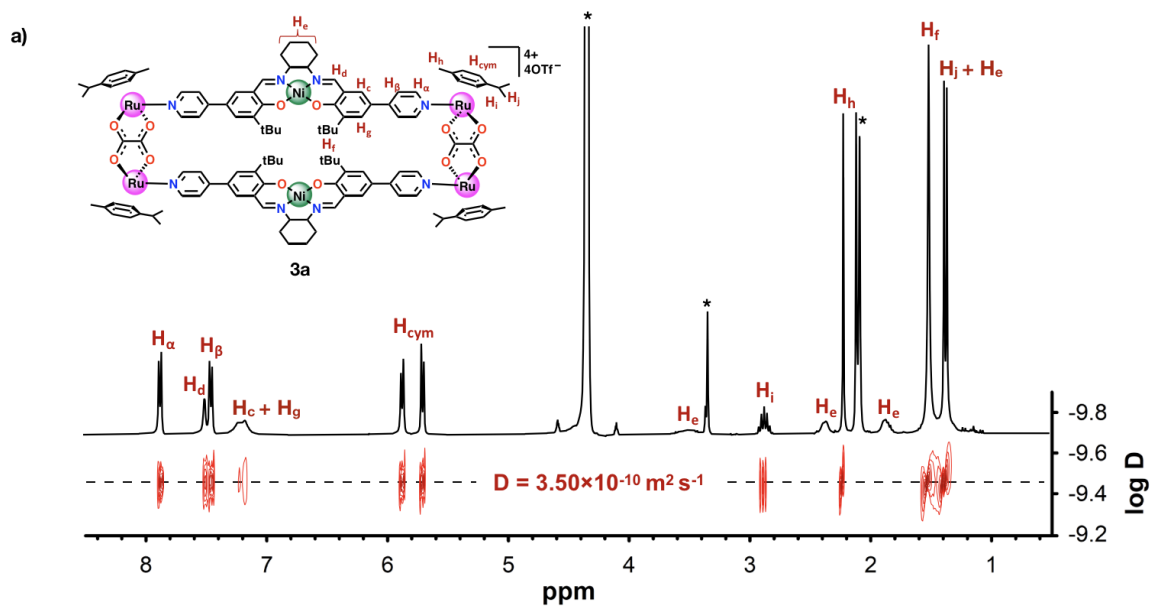




**Figure 3.**  $^1\text{H}$  NMR with corresponding  $^1\text{H}$  DOSY NMR of a) **3a** (4 mM) in  $\text{CD}_3\text{NO}_2$ ; b) **(3b)<sub>2</sub>** (4 mM) in  $\text{CD}_3\text{NO}_2$ , (\*) Solvents:  $\text{CH}_3\text{NO}_2$  (4.33 ppm) and  $\text{H}_2\text{O}$  (2.06 ppm); c) **3b** (2 mM) in  $\text{CD}_2\text{Cl}_2/\text{DMSO-d}_6$  (1:1), (\*) Solvents:  $\text{CH}_2\text{Cl}_2$  (5.55 ppm),  $\text{H}_2\text{O}$  (3.22 ppm) and DMSO (2.50 ppm).

Characterizing the self-assembly process of ligand **1** with complex **2b** in solution is more complicated considering the possible interlocked nature of the resulting compound. The size of the **bis-Ru(naphtho)** acceptor (**2b**,  $\text{Ru}\cdots\text{Ru}$ : 8.3 Å) governs the possible topologies involved in coordination-driven self-assembly, leading to the formation of a  $\text{M}_2\text{L}_2$  rectangle (**3b**) or to the interlocking of the  $\text{M}_2\text{L}_2$  fragments into a [2]catenane (**(3b)<sub>2</sub>**), as observed in the solid-state. The  $^1\text{H}$  NMR spectrum of **(3b)<sub>2</sub>** in nitromethane- $\text{d}_3$  at 4 mM (Figure 3b) presents a complex set of signals, suggesting the formation of a [2]catenane, or a mixture of species. However, a single alignment of the signals is observed in the  $^1\text{H}$  DOSY NMR spectrum, which supports a discrete self-assembly with  $D_{\text{NMR}} = 2.41 \times 10^{-10} \text{ m}^2 \text{ s}^{-1}$ , and which equates to a  $R_h$  value of 14.9 Å (see Table S3). In addition to nitromethane- $\text{d}_3$ , self-assembly to the [2]catenane **(3b)<sub>2</sub>** also occurs in  $\text{CD}_2\text{Cl}_2$  (See SI – Figure S14 for  $^1\text{H}$  DOSY NMR spectra). The hydrodynamic radii for **(3b)<sub>2</sub>**, in the above-mentioned solvents, were calculated from the diffusion coefficients using the Stokes-Einstein equation<sup>[82]</sup> (Table S3), and as expected from their respective geometry, the  $R_h$  values for **3a** (10.4 Å) are smaller in comparison to **(3b)<sub>2</sub>**, (14.6-14.9 Å).

Interestingly, under dilute conditions in  $\text{CH}_3\text{OH}$  (<0.1 mM) the coordination-driven self-assembly of **1** and **2b**, results in the majority formation of **3b** – an  $\text{M}_2\text{L}_2$  rectangular metallacycle. Conversion of **(3b)<sub>2</sub>** into **3b** with dilution is reversible upon re-concentration (Figure S15). This behavior is also supported by a concentration-dependent ESI-FTICR mass spectrometry study on **(3b)<sub>2</sub>** which shows conversion to **3b** upon dilution of the  $\text{CH}_3\text{OH}$  solution from 1 mM to 0.02 mM (Figure S3). Both solvent and concentration have been reported previously to have an effect on the formation of interlocked assemblies with *p*-cymene *bis*-Ru acceptors.<sup>[31,36,80,83,84]</sup> Conversion of **(3b)<sub>2</sub>** to **3b** also occurs upon dilution of a  $\text{CD}_3\text{NO}_2$  solution (Figure S16), and addition of  $\text{DMSO-d}_6$  into a  $\text{CD}_2\text{Cl}_2$  solution of **(3b)<sub>2</sub>** (Figure S18). However, interlocked **(3b)<sub>2</sub>** remains intact upon dilution of a  $\text{CD}_2\text{Cl}_2$  solution from 2.5 - 0.05 mM (Figure S19). The  $^1\text{H}$  NMR spectrum assignment for **3b** in  $\text{CD}_2\text{Cl}_2/\text{DMSO-d}_6$  (1:1) at  $C = 2.5$  mM together with the DOSY NMR spectrum is shown in Figure 3c, which indicates a single alignment of signals. A DOSY experiment was completed under conditions where both **(3b)<sub>2</sub>** and **3b** are present (0.5 mM in  $\text{CD}_3\text{NO}_2$ ) in order to compare the associated diffusion rate and  $R_h$  values (Figure S17). A diffusion rate

of  $D_{\text{NMR}} = 2.41 \times 10^{-10} \text{ m}^2 \text{ s}^{-1}$  was determined for **(3b)<sub>2</sub>** and  $D_{\text{NMR}} = 2.79 \times 10^{-10} \text{ m}^2 \text{ s}^{-1}$  for **3b**, corresponding to  $R_h$  values of 14.9 Å and 12.8 Å, respectively (Table S3). Thus, the DOSY results show the expected decrease in the  $R_h$  for **3b** in comparison to interlocked **(3b)<sub>2</sub>**.

## Electrochemistry

The electrochemical properties of metalla-structures **3a** and **(3b)<sub>2</sub>** were investigated in  $\text{CH}_2\text{Cl}_2$  via cyclic voltammetry (CV) and differential pulse voltammetry (DPV), and were compared to their constituent components **2a**, **2b**, and ligand **1** as well as reference compound **4** (Table 1). While Ni salen derivatives usually exhibit reversible ligand-based redox processes, ligand **1** undergoes an irreversible oxidation at 0.88 V (Figure S28), due to intermolecular interaction between the oxidized molecule and the pyridyl substituents from additional Ni salen units via axial coordination, resulting in structural rearrangement and Ni(III) formation (*vide infra*).<sup>[72]</sup> Complex **4** can be considered as the monomer analogue of **3a** and **(3b)<sub>2</sub>** in which the pyridines are capped with Ru(en)(*p*-cym) (en = ethylenediamine) nodes to prevent intermolecular interactions upon oxidation and thus compare to the redox events for the Ni salen unit in the metallacycles, **3a** and **(3b)<sub>2</sub>**. The CV of **4** shows two quasi-reversible one-electron redox processes (Figure S29a), at 0.74 V and 1.20 V vs.  $\text{Fc}^+/\text{Fc}$  (as determined by DPV). These redox potentials are in agreement with a previously reported **Ni(Salen)<sup>CF<sub>3</sub></sup>** complex containing a *para*- $\text{CF}_3$  substituent of a similar electron-withdrawing ability and matching Hammett constant to *para*-pyridyl.<sup>[85]</sup>

**Table 1.** Redox potentials for **1**, **2b**, **3a**, and **(3b)<sub>2</sub>** vs.  $\text{Fc}^+/\text{Fc}$ <sup>a</sup> (1.0 mM (**1**), 0.5 mM (**2b**, **3a**, **4**), 0.25 mM (**(3b)<sub>2</sub>**), 0.1 M  $n\text{Bu}_4\text{PF}_6$ , scan rate 100 mV s<sup>-1</sup>,  $\text{CH}_2\text{Cl}_2$ , 298 K).

Compound	<sup>1</sup> $E_{1/2}$ (V)	<sup>2</sup> $E_{1/2}$ (V)	<sup>3</sup> $E_{1/2}$ (V)	<sup>4</sup> $E_{1/2}$ (V)
Ni(Salen) <sup>pPy</sup> ( <b>1</b> )	-	-	0.88 <sup>[b]</sup>	-
<b>4</b> <sup>[c]</sup>	-	-	0.74 (85)	1.20 <sup>[d]</sup>
<b>3a</b>	-	-	0.85 (140)	-
<b>2b</b> <sup>[e]</sup>	-	-	0.25 <sup>[f]</sup>	0.62 <sup>[f]</sup>
<b>2b + pyridine</b> <sup>[e]</sup>	-1.31 (170)	-0.90 (160)	0.85 <sup>[f]</sup>	-
<b>(3b)<sub>2</sub></b>	-1.34 (180)	-0.87 (160)	0.82 (160)	1.24 (160)

<sup>a</sup>Peak-to-peak differences in brackets ( $|E_{\text{pa}} - E_{\text{pc}}|$  in mV). Peak-to-peak difference for the  $\text{Fc}^+/\text{Fc}$  couple at 298 K is 200 mV (**1**); 115 mV (**4**), 220 mV (**2b**), 160 mV (**3a**); 150 mV (**(3b)<sub>2</sub>**); <sup>b</sup>Irreversible, see Figure S28; <sup>c</sup>in  $\text{CH}_2\text{Cl}_2/\text{CH}_3\text{NO}_2$  (9:1); <sup>d</sup>determined by DPV; <sup>e</sup>0.1 M  $n\text{Bu}_4\text{ClO}_4$ , see Figure S31b; <sup>f</sup> $E_{\text{pa}}$  only. Note that **2a** does not show any redox processes in the electrochemical window.

Cyclic voltammetry of **3a** (Figure 4a) reveals only a single quasi-reversible redox process ( $E_{1/2} = 0.85$  V vs.  $\text{Fc}^+/\text{Fc}$ ) that is characterized as a one-electron oxidation of each salen unit (overall a two-electron process), as determined by the chemical oxidation experiments (*vide infra*). The low solubility of this metallacycle in  $\text{CH}_2\text{Cl}_2$  precludes using scan-rate dependence measurements (Figure S30a) to approximate the number of electrons transferred. Additionally, by running CV of **3a** in  $\text{CH}_3\text{NO}_2$  two one-electron processes of each salen are observed with the small difference in potentials indicating little interaction of these redox processes (Figure S30b). In order to rule out *bis*-Ru pillar (**2a** moiety) participation in the oxidation events, the CV of **2a** alone and with excess pyridine (Figure S31a) revealed no redox processes in the range of the couple for **3a**, supporting the previous assignment. The pyridine-ligated **2a** was studied to mimic the Ru coordination sphere in the metallacycle **3a**.

In contrast to **3a**, the CV of **(3b)<sub>2</sub>** in  $\text{CH}_2\text{Cl}_2$  shows four separate redox events (Figure 4b): two quasi-reversible reductions (-1.34 V and -0.87 V) and two quasi-reversible oxidations (0.82 V and 1.24 V). The concentration-dependence of the  $^1\text{H}$  NMR spectrum for **(3b)<sub>2</sub>** was investigated in  $\text{CD}_2\text{Cl}_2$  showing that the catenane does not dissociate in the concentration range 2.5 – 0.05 mM (Figure S19). It should be noted that the peak shape of the redox process at  $^3E_{1/2} = 0.82$  V suggests overlapped couples (see Figure S32 for DPV). Structurally, **(3b)<sub>2</sub>** is composed of four Ni salen units and four *bis*-Ru pillars. The first oxidation process ( $^3E_{1/2}$ ) was determined to be an eight-electron transfer, based on the chemical oxidation experiments. Peak height comparison of each redox process (Figure 4b), shows that each reduction (-1.34 and -0.87 V) is a four-electron process, which is in agreement with two sets of four Ru(II) to Ru(I) reductions.<sup>[86]</sup> To further assign the identity of the first oxidation event, the CV of **2b** was collected alone and with excess pyridine (Figure S31b). Two oxidation processes at much lower potentials of 0.25 V and 0.62 V were observed for **2b**, however, addition of excess pyridine shifted the oxidation to 0.85 V, matching that of **(3b)<sub>2</sub>**. We assign the oxidation event for the pyridine adduct of **2b** to the naphthoquinonato moiety (see calculation section), with the shift to higher potential in comparison to **2b** due to the 2+ charge of the pyridine adduct. We therefore conclude that the redox process at 0.82 V for **(3b)<sub>2</sub>** can be assigned to four one-electron oxidations of each salen unit and four additional one-electron oxidations of each *bis*-Ru pillar.

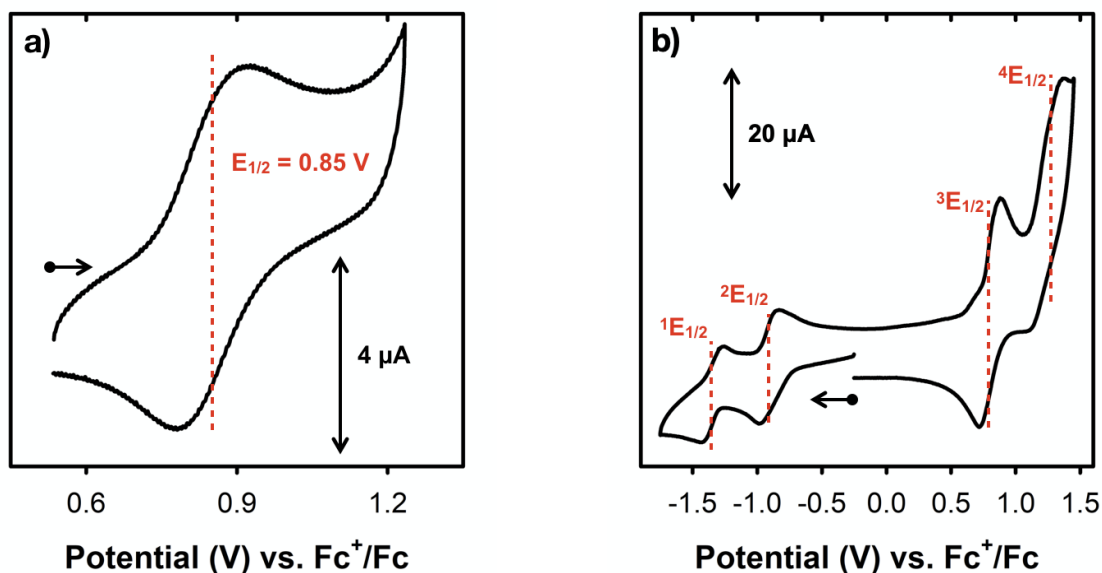


**Figure 4.** Cyclic voltammogram of a) **3a** (0.50 mM, 100 mV s<sup>-1</sup>), b) **(3b)<sub>2</sub>** (0.25 mM, 100 mV s<sup>-1</sup>), Conditions: 0.1 M <sup>n</sup>Bu<sub>4</sub>PF<sub>6</sub> in CH<sub>2</sub>Cl<sub>2</sub> at 298 K.

### Electron Paramagnetic Resonance Spectroscopy

Room temperature X-band EPR measurements were used to further characterize the electronic structure of the oxidized systems, **3a** and **(3b)<sub>2</sub>**, via chemical oxidation using an aminium radical oxidant, [N(C<sub>6</sub>H<sub>3</sub>Br<sub>2</sub>)<sub>3</sub>]<sup>•+</sup>[SbF<sub>6</sub>]<sup>-</sup> ( $E_{1/2} = 1.14$  V vs. Fc<sup>+</sup>/Fc).<sup>[87]</sup> It is worth mentioning that [**1**]<sup>+</sup> was characterized via EPR at 100 K in CH<sub>2</sub>Cl<sub>2</sub>, and showed an isotropic signal ( $g_{ave} = 2.141$ ) confirming the formation of a Ni(III) species upon intermolecular coordination of *p*-pyridyl groups (*vide infra*).<sup>[72]</sup> Solution EPR measurement of [**3a**]<sup>2•+</sup> in CH<sub>2</sub>Cl<sub>2</sub> (Figure S33) reveals a ligand radical signal at  $g_{iso} = 2.065$ , with a deviation of the  $g$  value from the free electron value ( $g_e = 2.0023$ ) due to the metal contribution to the SOMO.<sup>[85,88]</sup> The low intensity of the signal is due to the limited solubility of **3a** and [**3a**]<sup>2•+</sup> in CH<sub>2</sub>Cl<sub>2</sub>, compounded with the slow decay of [**3a**]<sup>2•+</sup> in solution. A sample of **2a** in the presence of the aminium oxidant was evaluated via EPR spectroscopy as well (Figure S36, inset). As confirmed by chemical oxidation experiments (*vide infra*), no oxidation of **2a** was observed, instead, the EPR spectrum shows a signal due to the oxidant ([N(C<sub>6</sub>H<sub>3</sub>Br<sub>2</sub>)<sub>3</sub>]<sup>•+</sup>[SbF<sub>6</sub>]<sup>-</sup>) with a  $g$  value of 2.007, matching the previously published report.<sup>[89]</sup> This evidence further supports only salen ligand oxidation in [**3a**]<sup>2•+</sup>.

In contrast to **2a**, solution EPR measurement of the oxidized *bis*-Ru(naphtho) complex, **[2b]<sup>+</sup>**, shows features consistent with ligand radical formation with a  $g_{\text{ave}}$  value of 2.007 and  $\Delta g = 0.085$  (Figure 5a, Table 2). Only a slight deviation from the free electron  $g_e$  value indicates a dominant organic radical character. Similar *bis*-Ru complexes bridged by the naphthazarin ligand were reported to form Ru(II)-semiquinone radical complexes with  $g_{\text{iso}}$  values of ca. 2.003 and exhibiting small  $g$ -anisotropy ( $\Delta g = 0.058\text{--}0.064$ ).<sup>[90,91]</sup> Ru-based oxidation is expected to lead to much larger  $g$ -anisotropy (i.e., broader signals).<sup>[92]</sup> Furthermore, the solution spectrum of **[2b]<sup>+</sup>** displays hyperfine coupling that was simulated in the fast-motion regime to four <sup>1</sup>H nuclear spins ( $I = 1/2$ ); <sup>99/101</sup>Ru contribution was not included in the simulation as no satellite hyperfine coupling is observed in the spectrum (<sup>99/101</sup>Ru: 12.7% and 17.0% abundance, respectively;  $I = 5/2$ ).<sup>[93]</sup> Finally, the electronic structure of the interlocked metallacycle **[(3b)<sub>2</sub>]<sup>8+</sup>** was analyzed to evaluate the locus of oxidation. Solution EPR measurement of **[(3b)<sub>2</sub>]<sup>8+</sup>** in CH<sub>2</sub>Cl<sub>2</sub> (Figure 5b, black) reveals a complex spectrum, which displays a combination of spectral features from two components: representing the oxidation of the salen unit (component 1,  $g_{\text{ave}} = 2.025$ ) and the *bis*-Ru pillar (component 2,  $g_{\text{ave}} = 2.001$ ) in a simulation shown in Figure 5b (red).<sup>[72]</sup> The EPR spectrum of **[4]<sup>+</sup>** (see Figure S34) represents the oxidation of the salen unit ( $g_{\text{ave}} = 2.051$ ) and the  $g_{\text{ave}}$  value calculated for component 2 is in agreement with ligand-based oxidation, similar to **[2b]<sup>+</sup>**. The deviation of the  $g$  values for **[4]<sup>+</sup>** and component 1 from the free electron  $g_e$  value is once again due to the metal (i.e., Ni) contribution to the SOMO.<sup>[85,88]</sup> However, metallacycle assembly slightly shifts the  $g$  value for the component radicals in comparison to the monomer counterparts (**[4]<sup>+</sup>** and **[2b]<sup>+</sup>**) potentially due to the sterics of the metallacycle. This suggests that ligands from the four Ni salen units and four *bis*-Ru pillars comprising the metallacycle are oxidized, forming **[(3b)<sub>2</sub>]<sup>8+</sup>**.

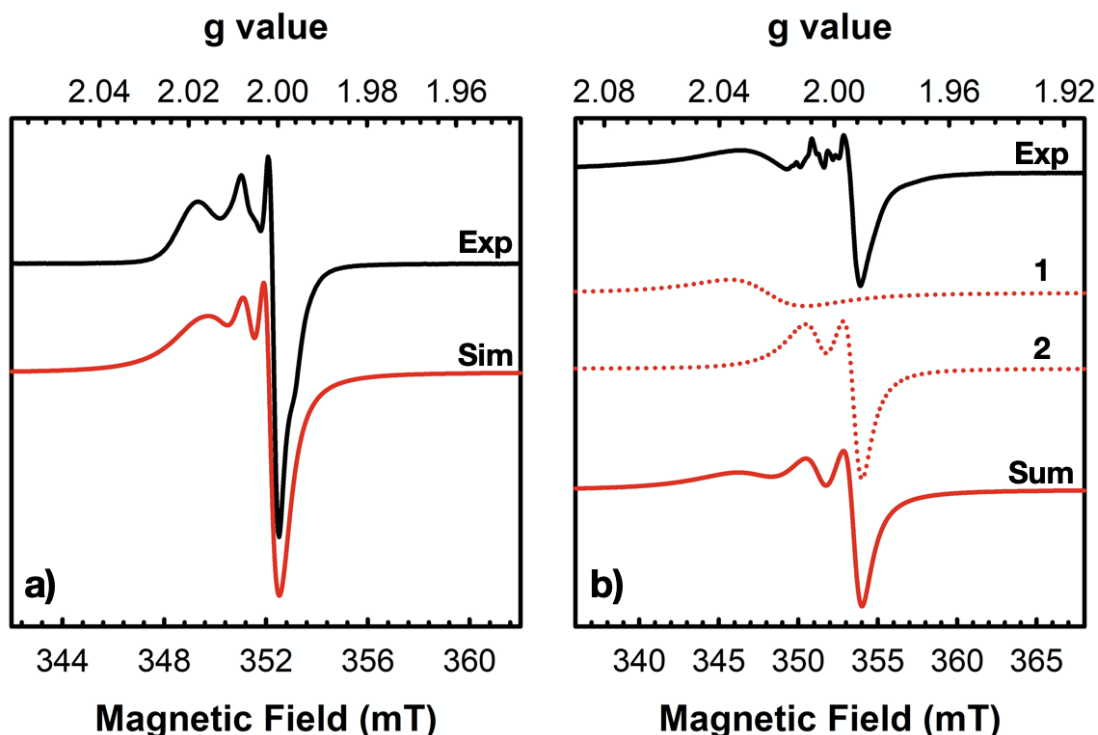


**Figure 5.** a) EPR of  $[2b]^+$  (2.8 mM, black solid line) in  $CH_2Cl_2$  at 298 K ( $g_{ave} = 2.007$ , simulation: red solid line); b) EPR of  $[(3b)_2]^{8+}$  (0.5 mM, black solid line) in  $CH_2Cl_2$  at 298 K (component 1:  $g_{ave} = 2.025$  (red dashed line), component 2:  $g_{ave} = 2.001$  (red dashed line), simulation sum (red solid line)); Conditions: frequency = 9.86 GHz, power = 2.0 mW, modulation frequency = 100 kHz, modulation amplitude = 0.1 mT.

**Table 2.** X-Band EPR simulation parameters for  $[4]^+$ ,  $[2b]^+$  and  $[(3b)_2]^{8+}$ .

Complex	Components	$g_1$	$g_2$	$g_3$	$g_{ave}$	$AH_1$ [MHz]
$[4]^+$ <sup>a,b</sup>	-	2.062	2.049	2.041	2.051	-
$[2b]^+$ <sup>c</sup>	-	2.054	1.999	1.969	2.008	156, 67, 28, 13
$[(3b)_2]^{8+}$ <sup>d</sup>	1	2.092	1.997	1.986	2.025	-
$[(3b)_2]^{8+}$ <sup>e</sup>	2	2.051	1.965	1.986	2.001	136, 71, 64, 43

<sup>a</sup>See Figure S34 for experimental data; line-broadening parameters (lwpp): <sup>b</sup>[0.74 3.70], <sup>c</sup>[0.1 0.05], <sup>d</sup>[0.5 4.5], <sup>e</sup>[0.001 0.001];

## Electronic Spectroscopy

Chemical oxidation of **1** using the aminium radical oxidant,  $[N(C_6H_3Br_2)_3]^{•+}[SbF_6]^-$  ( $E_{1/2} = 1.14$  V vs.  $Fc^+/Fc$ )<sup>[87]</sup> in dichloromethane at room temperature (Figure S35a) results

in no NIR transitions, with the only band at 20,000 cm<sup>-1</sup> indicative of metal-based oxidation to form a Ni<sup>III</sup> complex, further evidenced by EPR analysis (*vide supra*:  $g_{ave} = 2.141$ ).<sup>[72]</sup> Therefore, **4** was designed to have terminal pyridine groups capped by the Ru complex ([Ru(en)(p-cym)OTf][OTf]) in order to efficiently characterize and compare the electronic structure of the oxidized metallacycles to a monomeric analogue. The electronic spectrum of [4]<sup>•+</sup> shows the evolution of two broad low energy bands at 8,800 and 4,400 cm<sup>-1</sup> (Figure S35b), the energy of the NIR bands is in agreement with ligand-based oxidation, matching the previously characterized ligand radical IVCT bands for [Ni(Salen)<sup>CF<sub>3</sub></sup>]<sup>•+</sup> and [Ni(Salen)<sup>pPy</sup>]<sup>•+</sup> units in a Pd-containing square.<sup>[72,85]</sup>

**Table 3.** Spectroscopic properties of [4]<sup>•+</sup>, [3a]<sup>2•+</sup> and [(3b)<sub>2</sub>]<sup>8•+</sup>.

Metallacycle	$\nu_{max}$ [cm <sup>-1</sup> ] ( $\epsilon$ [M <sup>-1</sup> cm <sup>-1</sup> ])	$\nu_{max}$ [cm <sup>-1</sup> ] ( $\epsilon$ [M <sup>-1</sup> cm <sup>-1</sup> ])	$\Delta\nu_{1/2}$ (Experimental)	$\Delta\nu_{HTL}$ (Calculated) <sup>a</sup>
[4] <sup>•+</sup>	8,800 (2,000)	4,400 (5,000)	750	3,150
[3a] <sup>2•+</sup>	8,800 (8,500)	4,800 (18,000)	1,000	3,300
[(3b) <sub>2</sub> ] <sup>8•+</sup>	8,800 (37,000)	4,600 (66,000)	1,000	3,250

<sup>a</sup>  $\Delta\nu_{HTL} = \sqrt{16\ln 2RT\nu_{max}}$ . Where  $\Delta\nu_{HTL}$  = peak width at half height for the high temperature limit (in cm<sup>-1</sup>),  $R$  = gas constant (8.3145 J K<sup>-1</sup> mol<sup>-1</sup>),  $T$  = temperature (in K),  $\nu_{max}$  = energy of the band (in cm<sup>-1</sup>).

Chemical oxidation of **3a** in CH<sub>2</sub>Cl<sub>2</sub> at room temperature (Figure 6a) results in the formation of intense slightly broadened bands (see Table 3) in the NIR region, indicative of salen ligand radical formation. An equimolar addition of the aminium oxidant to **2a**, results in no reaction as evidenced by UV-vis-NIR and EPR (Figure S36, confirmed by EPR, *vide supra*).<sup>[89]</sup> This further supports that only the two salen units are oxidized in **3a** to form [3a]<sup>2•+</sup>.

Oxidation of (3b)<sub>2</sub> (Figure 6b) with eight equivalents of oxidant also results in the formation of intense and broad NIR bands at 4,600 and 8,800 cm<sup>-1</sup> (Table 3), with a shoulder peak at ca. 11,000 cm<sup>-1</sup>. In order to assign the loci of oxidation in [(3b)<sub>2</sub>]<sup>8•+</sup>, oxidation of **2b** was investigated as well. Spectral analysis of **2b** reveals two bands at 14,500 and 16,000 cm<sup>-1</sup> (Figure S37, black spectrum), indicative of intra/intermolecular  $\pi \rightarrow \pi^*$  transitions mixed with metal-to-ligand charge transfer (MLCT) transitions.<sup>[46,94]</sup> These bands are also present in the neutral and oxidized forms of (3b)<sub>2</sub>. An oxidation titration with one equivalent of the oxidant results in three isosbestic points (14,000, 17,000 and 20,500 cm<sup>-1</sup>) and formation of [2b]<sup>•+</sup> (see Figure S37, red spectrum). A new band at 11,000 cm<sup>-1</sup> is assigned as an intra-ligand transition of the ligand radical, corroborated by

a literature example of an organometallic *bis*-Ru complex bridged by anthrasemiquinone, resembling similar spectral features pre- and post-oxidation.<sup>[91]</sup> Furthermore, DFT calculations on  $[2b]^+$  reveal delocalization of the unpaired electron across the naphthazarin ligand scaffold, and TD-DFT calculations predict a number of transitions of high intensity in the energy range of the new band at 11,000  $\text{cm}^{-1}$  (Figure S37, green bars and inset). Combined with EPR analysis (*vide supra*), ligand-based oxidation is observed in **2b**, leading to the formation of  $[2b]^{++}$ . This further supports that oxidation of **3b** is fully ligand-based, and each salen and pillar unit is oxidized in  $[(3b)_2]^{8+}$ .

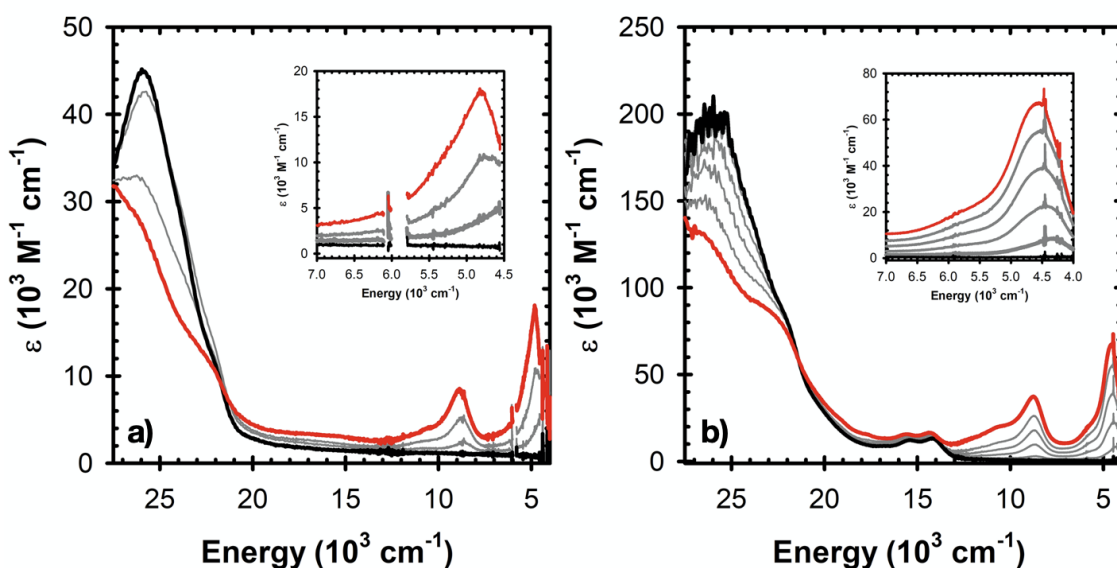


**Figure 6.** a) Electronic spectra of chemical oxidation of **3a** (0.01 mM, black) to  $[3a]^{2+}$  (red), Inset: lowest energy NIR band; b) Electronic spectra of chemical oxidation of  $(3b)_2$  (0.1 mM, black) to  $[(3b)_2]^{8+}$  (red), Inset: lowest energy NIR band; Conditions: in  $\text{CH}_2\text{Cl}_2$ , at 298 K, titrated with 16 mM (**3a**) and 19 mM  $(3b)_2$   $[\text{N}(\text{C}_6\text{H}_3\text{Br}_2)_3]^+[\text{SbF}_6]^-$  as oxidant. Grey spectra represent aliquot additions of the oxidant. Solvent peaks were removed for clarity (5,800-6,000  $\text{cm}^{-1}$ ).

The reversibility of the oxidation and the stability of the oxidized species were investigated through stepwise *in situ* reduction and re-oxidation (Figure S38).  $[3a]^{2+}$  and  $[(3b)_2]^{8+}$  were reduced with two and eight molar equivalents of decamethylferrocene ( $\text{FeCp}^*_2$ ;  $E_{1/2} = -0.48$  V in dichloromethane<sup>[87]</sup>), respectively, returning to the original spectra (Figure S38, black dashed lines). The samples of  $[3a]^{2+}$  and  $[(3b)_2]^{8+}$  were regenerated after re-oxidation with 90% and 70% recovery, respectively, as determined by the intensity of the lowest energy bands (Figure S38, insets).



Characterization of the energy, intensity, and shape of the NIR bands can inform the assignment of the degree of localization in the mixed-valence systems. Class III delocalized systems display sharp ( $\Delta\nu_{1/2} \leq 2,000 \text{ cm}^{-1}$ ) and intense ( $\epsilon \geq 5,000 \text{ M}^{-1} \text{ cm}^{-1}$ ) IVCT bands that are solvent independent.<sup>[95]</sup> The Hush equation<sup>[95,96,97]</sup> was used to evaluate the lowest energy NIR bands for  $[\mathbf{4}]^{\bullet+}$ ,  $[\mathbf{3a}]^{2\bullet+}$ , and  $[(\mathbf{3b})_2]^{8\bullet+}$  (see Table 3). The experimental  $\Delta\nu_{1/2}$  values fall under the minimum bandwidth predicted for the high-temperature limit ( $\Delta\nu_{\text{HTL}}$ ), designating the oxidized complexes as Class III delocalized systems. This in turn matches previously characterized  $[\text{Ni}(\text{Salen})^{\text{R}}]^{\bullet+}$  (where R = <sup>t</sup>Bu and CF<sub>3</sub>) complexes that also displayed experimental  $\Delta\nu_{1/2}$  values 30% lower than  $\Delta\nu_{\text{HTL}}$ .<sup>[85,98]</sup>

The intensity of the low energy bands for  $[(\mathbf{3b})_2]^{8\bullet+}$  are comparable with the previously reported square metallacycle, also containing four oxidized salen units.<sup>[72]</sup> The difference in the intensities of the NIR bands for  $[\mathbf{4}]^{\bullet+}$  and  $[\mathbf{3a}]^{2\bullet+}$  is likely due to their limited solubility in CH<sub>2</sub>Cl<sub>2</sub>. It should be noted that 10 % nitromethane in CH<sub>2</sub>Cl<sub>2</sub> was used to improve solubility in the oxidation experiment of **4**, however for a Class III delocalized system, the solvent should have a limited effect on the IVCT bands.

Assuming the metallacycle structure of both **3a** and  $(\mathbf{3b})_2$  are maintained in solution upon oxidation, and based on our previous work investigating excited state NIR band coupling in comparable systems,<sup>[59,63]</sup> the exciton model predicts that both oxidized metallacycles will display a blue-shift of the ligand radical IVCT band upon oxidation (Figure 2), in comparison to the monomeric analogue ( $[\mathbf{4}]^{\bullet+}$ ). The extent of the blue-shift depends on the distance and angular orientation between the transition dipole moments in the metallacycles,  $[\mathbf{3a}]^{2\bullet+}$  and  $[(\mathbf{3b})_2]^{8\bullet+}$ , in comparison to  $[\mathbf{4}]^{\bullet+}$ .<sup>[59,63,70,71]</sup> For the metallacycle  $[\mathbf{3a}]^{2\bullet+}$ , where the two salen units are cofacially aligned and 3.84 Å apart (Ni – Ni distance for **3a** in the solid state), a 400 cm<sup>-1</sup> blue-shift vs.  $[\mathbf{4}]^{\bullet+}$  is observed, consistent with the exciton model (Figures 1 and 7). This compares favourably to a previously reported Ni salen dimer complex, exhibiting a similar shift (330 cm<sup>-1</sup>) with two salen units cofacially aligned and 3.98 Å apart.<sup>[59]</sup>

For the metallacycle  $(\mathbf{3b})_2$ , the approximate orientation between the salen units in the two interlocked rectangles is ca. 50° (Figure 2b) in the neutral form, and a blue-shift of 200 cm<sup>-1</sup> for the IVCT band is observed for  $[(\mathbf{3b})_2]^{8\bullet+}$  vs.  $[\mathbf{4}]^{\bullet+}$  (Figure 7). This is in accordance with the exciton model in which the chromophores are stacked, but not

cofacially aligned (Figure 1).<sup>[71]</sup> Additionally, no shift is observed in the IVCT bands for  $[4]^{*+}$  in comparison to the supramolecular square containing four  $[\text{Ni}(\text{Salen})^{\text{PPy}}]^{*+}$  units due to the geometrical arrangement of the square, and larger distance between chromophores.<sup>[72]</sup>

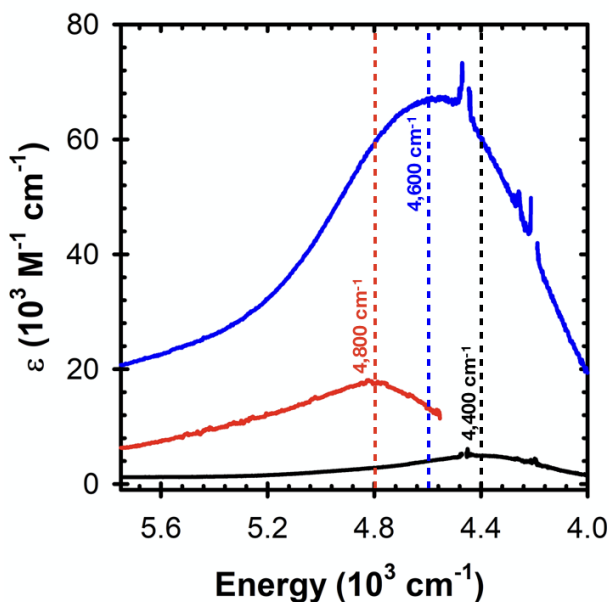


**Figure 7.** Electronic spectra comparison of the lowest energy bands for  $[4]^{*+}$  (black),  $[3a]^{2*+}$  (red), and  $[(3b)_2]^{8*+}$  (blue). The  $\nu_{\text{max}}$  values are traced with dashed lines,  $[4]^{*+}$  (black),  $[3a]^{2*+}$  (red), and  $[(3b)_2]^{8*+}$  (blue). Solvent peaks were removed for clarity (4,000-4,560  $\text{cm}^{-1}$ ).

## Theoretical Calculations

We further investigated **4** and **3a** and the oxidized species  $[4]^+$  and  $[3a]^{2+}$  by Density Functional Theory (DFT) to provide insight on the geometric and electronic structure as well as excited state coupling for the oxidized forms. Calculations on  $(3b)_2$  and  $[(3b)_2]^{8*+}$  were not attempted due to the increased complexity of the interlocked metallacycle. Oxidation of **4** is predicted to result in a delocalized ligand radical  $[4]^{*+}$ , matching the experimental results. The spin density plot is shown in Figure 8a, with minimal density on the Ru moieties. In agreement with previous reports,<sup>[61,62,99]</sup> ligand radical formation results in coordination sphere contraction due to removal of an electron from a predominantly ligand  $\pi^*$  orbital, and as a result  $[4]^{*+}$  is predicted to adopt a stepped

structure (Figure S39). Geometry optimization of **3a** incorporating dispersion effects<sup>[100]</sup> results in a rectangular metallacycle with coordination sphere metrical parameters within  $\pm 0.02$  Å of the X-ray data (Figure 8b). The Ni···Ni distance between the two salen units is predicted to be 3.75 Å, which is similar to the X-ray data (3.84 Å). Interestingly, without dispersion corrections the Ni···Ni distance is predicted to be 5.7 Å, suggesting that  $\pi$ - $\pi$  stacking is an important determinant of the metallacycle structure.

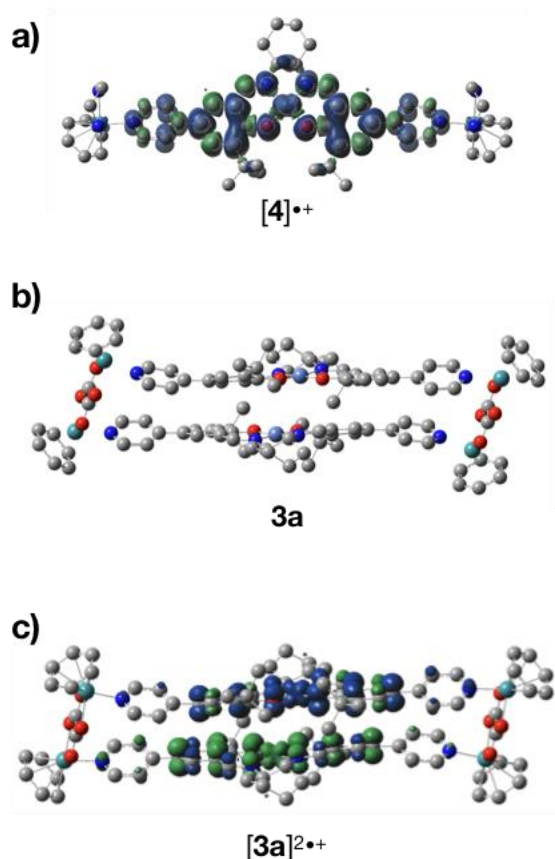


**Figure 8.** a) Spin density plot for  $[4]^{\bullet+}$ , b) DFT-optimized geometry for **3a**, and c) broken-symmetry spin density plot for  $[3a]^{2\bullet+}$ ; The Ni···Ni distance for **3a** is 3.75 Å and 3.79 Å for  $[3a]^{2\bullet+}$ . See Experimental Section for calculation details.

Geometry optimization calculations of  $[3a]^{2\bullet+}$  predict both triplet ( $S = 1$ ) and broken-symmetry (BS,  $S = 0$ ) solutions to be essentially energetically equivalent spin states (BS is predicted to be 0.04 kcal mol<sup>-1</sup> lower in energy), thus a non-interacting biradical description is appropriate.<sup>[59,101]</sup> Both the triplet and BS-optimized structures exhibit contracted coordination sphere bond lengths (Ni-O from 1.85 to 1.82 Å, and Ni-N from

1.85 to 1.84 Å) in agreement with the monomer analogue [4]<sup>•+</sup>. In addition, for both electronic states the predicted Ni···Ni distance only expands slightly from 3.75 Å to 3.79 Å upon bis-oxidation. Note that without added dispersion corrections significant distortion of the salen ligands occurs for the bis-oxidized forms with an expanded Ni···Ni distance of 11.1 Å. The spin density plot for the broken-symmetry solution for [3a]<sup>2•+</sup> (Figure 8c) shows radical delocalization across each of the salen moieties with minimal density on *bis*-Ru pillars, which agrees with the prediction for [4]<sup>•+</sup> and the experimental data.

Time-dependent DFT (TD-DFT) calculations on [4]<sup>•+</sup> and [3a]<sup>2•+</sup> were completed to investigate the donor and acceptor orbitals as well as NIR band energy shifts. For [4]<sup>•+</sup>, an intense NIR IVCT band is predicted at 5232 cm<sup>-1</sup> ( $f = 0.2661$ ), which is blue-shifted in comparison to the experimental data. The donor ( $\beta$ -HOMO) and acceptor ( $\beta$ -LUMO) orbitals are delocalized across the salen ligand (Figure S40). For [3a]<sup>2•+</sup>, TD-DFT calculations for both triplet (Figure S41) and BS solutions (Figure 9) predict two NIR bands, however only the high energy band has appreciable intensity. For the BS solution the predicted higher energy band at 5500 cm<sup>-1</sup> exhibits an increased intensity ( $f = 0.3872$ ) in comparison to [4]<sup>•+</sup>, while the lower energy band at 4708 cm<sup>-1</sup> is not predicted to have any intensity ( $f = 0.0000$ ), in line with the exciton model for a cofacial arrangement of chromophores. Experimentally, the NIR band intensity for [3a]<sup>2•+</sup> is *ca.* 4-fold in comparison to [4]<sup>•+</sup>, which is at least partially a result of the low solubility of [4]<sup>•+</sup> in CH<sub>2</sub>Cl<sub>2</sub>. The donor and acceptor orbitals for [3a]<sup>2•+</sup> are confined to the salen units and match the orbitals associated with the low energy transition of [4]<sup>•+</sup>; the predicted NIR bands are symmetric and antisymmetric linear combinations of  $\alpha$ -HOMO  $\rightarrow$   $\alpha$ -LUMO and  $\beta$ -HOMO  $\rightarrow$   $\beta$ -LUMO transitions of the salen radical units (Figure 9).<sup>[59,63]</sup> Finally, the experimental shift to higher energy (*ca.* 400 cm<sup>-1</sup>) for the NIR band of [3a]<sup>2•+</sup> in comparison to [4]<sup>•+</sup> matches  $\frac{1}{2}$  the predicted energy difference between the NIR bands in the TD-DFT calculation for [3a]<sup>2•+</sup> (396 cm<sup>-1</sup>). Thus, the TD-DFT calculations provide further evidence for excited-state interaction of the salen chromophores in [3a]<sup>2•+</sup> and that the cofacial arrangement of the salen units is maintained in the oxidized form.

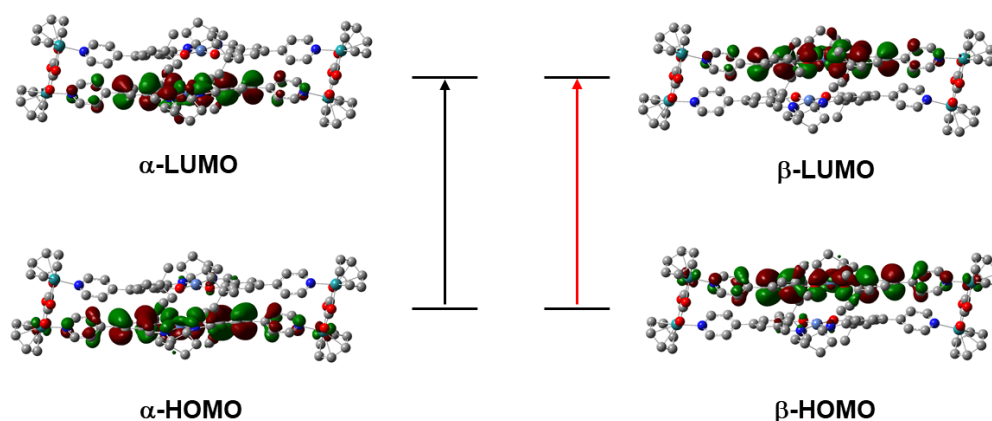


**Figure 9.** Predicted donor and acceptor orbitals for the broken-symmetry solution ( $S = 0$ ) of  $[3\mathbf{a}]^{2\bullet+}$ , associated with the calculated NIR transitions at 4708 ( $f = 0.0000$ ) and 5500  $\text{cm}^{-1}$  ( $f = 0.3872$ ) (black and red arrows;  $\alpha/\beta\text{-HOMO} \rightarrow \alpha/\beta\text{-LUMO}$ ).

## Conclusion

Coordination-driven self-assembly was employed in the design and synthesis of two metallacycles containing  $\text{Ni}(\text{Salen})^{\text{pPy}}$  (**1**) metalloligands and two *bis*-Ru(oxalato) (**2a**) and *bis*-Ru(naphtho) (**2b**) complexes as acceptors. Using these *bis*-Ru complexes provides a strategy for simple variation of the metallacycle cavity size and topology (e.g. interlocking). Characterization of the self-assembly process revealed a solvent and a concentration dependence in the assembly of  $(3\mathbf{b})_2$  (a catenane  $(\text{M}_2\text{L}_2)_2$  assembly) and **3b** (a non-interlocked,  $\text{M}_2\text{L}_2$  assembly). Even though, **3b** could not be isolated in the solid-state, it was characterized by high resolution mass spectrometry and select NMR spectroscopy techniques ( $^1\text{H}$  and 2D experiments, such as DOSY, COSY, HSQC, and HMBC). In addition, a new complex (**4**) was synthesized and studied as a monomeric analogue of the metallacycles, and its oxidation affords a ligand radical complex as evidenced by the generation of low energy IVCT bands at 8,800 and 4,400  $\text{cm}^{-1}$ . Oxidation of **3a** results in ligand-based oxidation of both metallosalen units to form  $[3\mathbf{a}]^{2\bullet+}$ , as characterized by low energy IVCT bands (8,800 and 4,800  $\text{cm}^{-1}$ ) and EPR spectroscopy ( $g_{\text{iso}} = 2.065$ ). However, oxidation of  $(3\mathbf{b})_2$  results in oxidation of all four salen and naphthazarin ligands (from the *bis*-Ru pillar), an overall 8-electron ligand radical-based process. UV-Vis-NIR and EPR spectroscopies corroborate this conclusion with low energy IVCT bands (8,800 and 4,600  $\text{cm}^{-1}$  for salen and 11,000  $\text{cm}^{-1}$  for Ru pillar) and a complex EPR spectrum for  $[(3\mathbf{b})_2]^{8\bullet+}$ , displaying combined spectral features of  $[2\mathbf{b}]^{\bullet+}$  and  $[4]^{\bullet+}$ .

Finally, both  $[3a]^{2+}$  and  $[(3b)_2]^{8+}$  exhibited blue-shifted IVCT bands (400 and 200  $\text{cm}^{-1}$ , respectively) in comparison to the monomeric analogue ( $[4]^{++}$ ), in agreement with the exciton model for cofacially-oriented chromophores (Figure 1). Computational studies of  $[3a]^{2+}$ , in comparison to  $[4]^{++}$ , predict a blue-shift and increase in NIR band intensity in agreement with the co-facial arrangement of the transition moment dipoles, further confirming the similarity of the solution state structure of the oxidized complex in comparison to the neutral form in the solid state. In future work we aim to probe how the presence of guest molecules influences the formation of rectangle (3b) and [2]catenane  $((3b)_2)$  in the neutral and oxidized forms.

## Acknowledgements

This work was supported by a Natural Sciences and Engineering Research Council (NSERC) Discovery Grant (RGPIN-2014-05240 T. S.). K. H. thanks Mitacs Canada for a Globalink Fellowship (FR32203) and the French national FT-ICR network for its financial support (FR 3624 CNRS). The authors gratefully acknowledge Prof. Charles Walsby for access to EPR. The authors are also thankful to Dr. Eric Ye, Simon Fraser University, for his assistance with DOSY NMR spectroscopy. Compute Canada is thanked for access to computational resources.

## References

1. A. Casini, B. Woods, M. Wenzel, *Inorg. Chem.* **2017**, *56*, 14715-14729.
2. R. Chakrabarty, P. S. Mukherjee, P. J. Stang, *Chem. Rev.* **2011**, *111*, 6810-6918.
3. T. R. Cook, P. J. Stang, *Chem. Rev.* **2015**, *115*, 7001-7045.
4. S. Datta, M. L. Saha, P. J. Stang, *Acc. Chem. Res.* **2018**, *51*, 2047-2063.
5. K. Harris, D. Fujita, M. Fujita, *Chem. Commun.* **2013**, *49*, 6703-6712.
6. B. Li, T. He, Y. Q. Fan, X. C. Yuan, H. Y. Qiu, S. C. Yin, *Chem. Comm.* **2019**, *55*, 8036-8059.
7. Y. Lu, H.-N. Zhang, G.-X. Jin, *Acc. Chem. Res.* **2018**, *51*, 2148-2158.
8. A. J. McConnell, C. S. Wood, P. P. Neelakandan, J. R. Nitschke, *Chem. Rev.* **2015**, *115*, 7729-7793.
9. E. G. Percastegui, T. K. Ronson, J. R. Nitschke, *Chem. Rev.* **2020**, *120*, 13480-13544.
10. Y. Sun, C. Y. Chen, J. B. Liu, P. J. Stang, *Chem. Soc. Rev.* **2020**, *49*, 3889-3919.
11. S. Bivaud, J. Y. Balandier, M. Chas, M. Allain, S. Goeb, M. Sallé, *J. Am. Chem. Soc.* **2012**, *134*, 11968-11970.

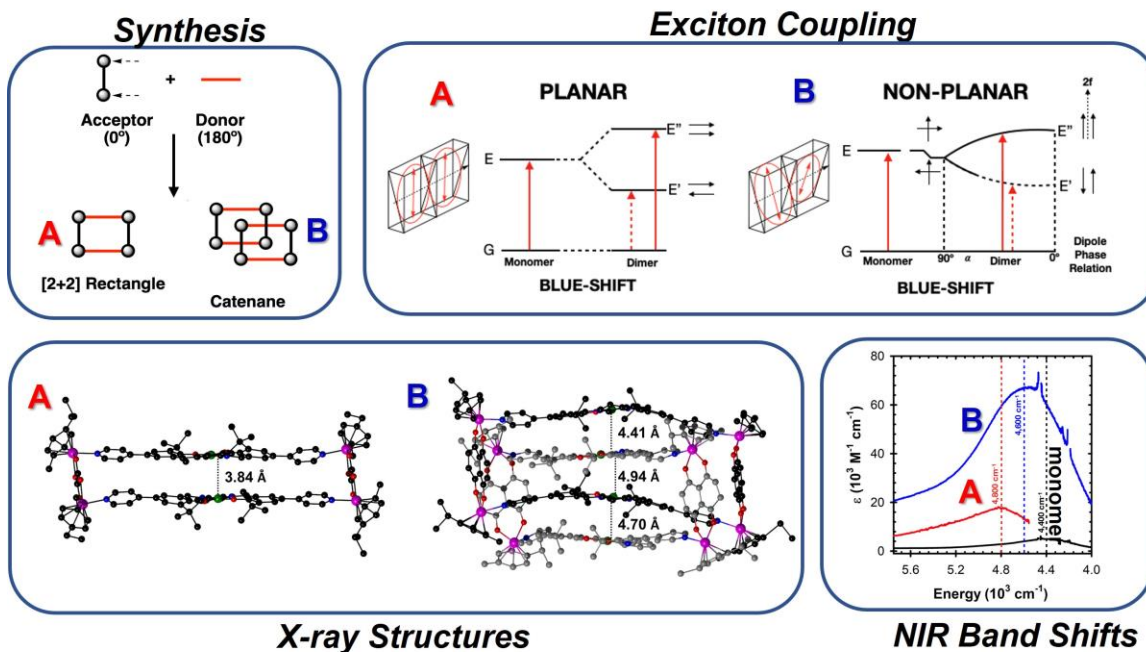
12. S. D. P. Fielden, D. A. Leigh, S. L. Woltering, *Angew. Chem. Int. Ed.* **2017**, *56*, 11166-11194.
13. W. X. Gao, H. J. Feng, B. B. Guo, Y. Lu, G. X. Jin, *Chem. Rev.* **2020**, *120*, 6288-6325.
14. L. R. Holloway, P. M. Bogie, R. J. Hooley, *Dalton Trans.* **2017**, *46*, 14719-14723.
15. S. L. Huang, Y. J. Lin, T. S. A. Hor, G. X. Jin, *J. Am. Chem. Soc.* **2013**, *135*, 8125-8128.
16. S. Pullen, G. H. Clever, *Acc. Chem. Res.* **2018**, *51*, 3052-3064.
17. B. Roy, R. Saha, A. K. Ghosh, Y. Patil, P. S. Mukherjee, *Inorg. Chem.* **2017**, *56*, 3579-3588.
18. S. Wang, T. Sawada, M. Fujita, *Chem. Commun.* **2016**, *52*, 11653-11656.
19. W. Wang, Y. X. Wang, H. B. Yang, *Chem. Soc. Rev.* **2016**, *45*, 2656-2693.
20. G. Y. Wu, L. J. Chen, L. Xu, X. L. Zhao, H. B. Yang, *Coord. Chem. Rev.* **2018**, *369*, 39-75.
21. S. Goeb, M. Sallé, *Acc. Chem. Res.* **2021**, *54*, 1043-1055.
22. B. H. Northrop, H. B. Yang, P. J. Stang, *Chem. Commun.* **2008**, 5896-5908.
23. K. E. Griffiths, J. F. Stoddart, *Pure Appl. Chem.* **2008**, *80*, 485-506.
24. W. L. Shan, Y. J. Lin, F. E. Hahn, G. X. Jin, *Angew. Chem. Int. Ed.* **2019**, *58*, 5882-5886.
25. J. E. M. Lewis, P. D. Beer, S. J. Loeb, S. M. Goldup, *Chem. Soc. Rev.* **2017**, *46*, 2577-2591.
26. K. Zhu, G. Baggi, S. J. Loeb, *Nat. Chem.* **2018**, *10*, 625-630.
27. J. E. Beves, J. J. Danon, D. A. Leigh, J. F. Lemonnier, I. J. Vitorica-Yrezabal, *Angew. Chem. Int. Ed.* **2015**, *54*, 7555-7559.
28. Z. Cui, Y. Lu, X. Gao, H. J. Feng, G. X. Jin, *J. Am. Chem. Soc.* **2020**, *142*, 13667-13671.
29. C. D. Pentecost, K. S. Chichak, A. J. Peters, G. W. V. Cave, S. J. Cantrill, J. F. Stoddart, *Angew. Chem. Int. Ed.* **2007**, *46*, 218-222.
30. C. Schouwey, J. J. Holstein, R. Scopelliti, K. O. Zhurov, K. O. Nagornov, Y. O. Tsybin, O. S. Smart, G. Bricogne, K. Severin, *Angew. Chem. Int. Ed.* **2014**, *53*, 11261-11265.
31. Y. H. Song, N. Singh, J. Jung, H. Kim, E. H. Kim, H. K. Cheong, Y. Kim, K. W. Chi, *Angew. Chem. Int. Ed.* **2016**, *55*, 2007-2011.
32. H. N. Zhang, W. X. Gao, Y. J. Lin, G. X. Jin, *J. Am. Chem. Soc.* **2019**, *141*, 16057-16063.
33. D. H. Kim, N. Singh, J. Oh, E. H. Kim, J. Jung, H. Kim, K. W. Chi, *Angew. Chem. Int. Ed.* **2018**, *57*, 5669-5673.
34. D. A. Leigh, J. J. Danon, S. D. P. Fielden, J.-F. Lemonnier, G. F. S. Whitehead, S. L. Woltering, *Nature Chem.* **2021**, *13*, 117-122.
35. H. J. Feng, W. X. Gao, Y. J. Lin, G. X. Jin, *Chem.-Asian J.* **2019**, *14*, 2712-2718.
36. T. Kim, N. Singh, J. Oh, E. H. Kim, J. Jung, H. Kim, K. W. Chi, *J. Am. Chem. Soc.* **2016**, *138*, 8368-8371.
37. Y. Lu, Y. X. Deng, Y. J. Lin, Y. F. Han, L. H. Weng, Z. H. Li, G. X. Jin, *Chem* **2017**, *3*, 110-121.
38. Y. Lu, Y. J. Lin, Z. H. Li, G. X. Jin, *Chinese Journal of Chemistry* **2018**, *36*, 106-111.
39. M. Frank, M. D. Johnstone, G. H. Clever, *Chem. Eur. J.* **2016**, *22*, 14104-14125.
40. S.-L. Huang, T. S. A. Hor, G.-X. Jin, *Coord. Chem. Rev.* **2017**, *333*, 1-26.
41. N. P. E. Barry, J. Furrer, B. Therrien, *Helv. Chim. Acta* **2010**, *93*, 1313-1328.
42. N. P. Barry, N. H. Abd Karim, R. Vilar, B. Therrien, *Dalton Trans.* **2009**, 10717-10719.

43. N. P. E. Barry, J. Furrer, J. Freudenreich, G. Süss-Fink, B. Therrien, *Eur. J. Inorg. Chem.* **2010**, 725-728.
44. V. Vajpayee, S. Bivaud, S. Goeb, V. Croué, M. Allain, B. V. Popp, A. Garci, B. Therrien, M. Sallé, *Organometallics* **2014**, 33, 1651-1658.
45. B. Therrien, G. Suss-Fink, P. Govindaswamy, A. K. Renfrew, P. J. Dyson, *Angew. Chem. Int. Ed.* **2008**, 47, 3773-3776.
46. V. Vajpayee, S. Lee, S. H. Kim, S. C. Kang, T. R. Cook, H. Kim, D. W. Kim, S. Verma, M. S. Lah, I. S. Kim, M. Wang, P. J. Stang, K. W. Chi, *Dalton Trans.* **2013**, 42, 466-475.
47. A. Mishra, S. Ravikumar, Y. H. Song, N. S. Prabhu, H. Kim, S. H. Hong, S. Cheon, J. Noh, K. W. Chi, *Dalton Trans.* **2014**, 43, 6032-6040.
48. T. Kim, H. S. Song, J. Singh, D. Kim, H. Kim, S. C. Kang, K.-W. Chi, *Inorg. Chim. Acta* **2018**, 482, 179-186.
49. A. Mishra, S. C. Kang, K.-W. Chi, *Eur. J. Inorg. Chem.* **2013**, 2013, 5222-5232.
50. V. Vajpayee, Y. H. Song, T. R. Cook, H. Kim, Y. Lee, P. J. Stang, K. W. Chi, *J. Am. Chem. Soc.* **2011**, 133, 19646-19649.
51. M. Wang, V. Vajpayee, S. Shanmugaraju, Y. R. Zheng, Z. Zhao, H. Kim, P. S. Mukherjee, K. W. Chi, P. J. Stang, *Inorg. Chem.* **2011**, 50, 1506-1512.
52. J. Y. Ryu, J. M. Lee, N. Van Nghia, K. M. Lee, S. Lee, M. H. Lee, P. J. Stang, J. Lee, *Inorg. Chem.* **2018**, 57, 11696-11703.
53. Y. Zhao, L. Zhang, X. Li, Y. Shi, R. Ding, M. Teng, P. Zhang, C. Cao, P. J. Stang, *Proc Natl Acad Sci USA* **2019**, 116, 4090-4098.
54. J. Y. Ryu, Y. J. Park, H. R. Park, M. L. Saha, P. J. Stang, J. Lee, *J. Am. Chem. Soc.* **2015**, 137, 13018-13023.
55. Y. F. Han, W. G. Jia, W. B. Yu, G. X. Jin, *Chem. Soc. Rev.* **2009**, 38, 3419-3434.
56. A. Dubey, Y. J. Jeong, J. H. Jo, S. Woo, D. H. Kim, H. Kim, S. C. Kang, P. J. Stang, K.-W. Chi, *Organometallics* **2015**, 34, 4507-4514.
57. N. J. Hestand, F. C. Spano, *Acc. Chem. Res.* **2017**, 50, 341-350.
58. T.-M. Liu, J. Conde, T. Lipiński, A. Bednarkiewicz, C.-C. Huang, *NPG Asia Mater.* **2016**, 8, e295.
59. R. M. Clarke, T. Jeen, S. Rigo, J. R. Thompson, L. G. Kaake, F. Thomas, T. Storr, *Chem. Sci.* **2018**, 9, 1610-1620.
60. W. Kaim, *Coord. Chem. Rev.* **2011**, 255, 2503-2513.
61. R. M. Clarke, K. Herasymchuk, T. Storr, *Coord. Chem. Rev.* **2017**, 352, 67-82.
62. T. Storr, E. C. Wasinger, R. C. Pratt, T. D. P. Stack, *Angew. Chem. Int. Ed.* **2007**, 46, 5198-5201.
63. T. J. Dunn, L. Chiang, C. F. Ramogida, K. Hazin, M. I. Webb, M. J. Katz, T. Storr, *Chem. Eur. J.* **2013**, 19, 9606-9618.
64. R. F. Winter, *Curr. Opin. Electrochem.* **2018**, 8, 14-23.
65. V. Croue, S. Goeb, M. Sallé, *Chem. Commun.* **2015**, 51, 7275-7289.
66. L. Xu, Y. X. Wang, L. J. Chen, H. B. Yang, *Chem. Soc. Rev.* **2015**, 44, 2148-2167.
67. R. Plessius, V. Deij, J. N. H. Reek, J. I. van der Vlugt, *Chem. Eur. J.* **2020**, 26, 13241-13248.
68. R. Plessius, N. Orth, I. Ivanovic-Burmazovic, M. A. Siegler, J. N. H. Reek, J. I. van der Vlugt, *Chem. Commun.* **2019**, 55, 12619-12622.
69. N. M. Bonanno, Z. Watts, C. Mauws, B. O. Patrick, C. R. Wiebe, Y. Shibano, K. Sugisaki, H. Matsuoka, D. Shiomi, K. Sato, T. Takui, M. T. Lemaire, *Chem. Comm.* **2021**, 57, 6213-6216.
70. M. Kasha, *Radiation Research* **1963**, 20, 55-71.
71. M. Kasha, H. R. Rawls, A. El-Bayoumi, *Pure Appl. Chem.* **1965**, 11, 371-392.



72. K. Herasymchuk, J. J. Miller, G. A. MacNeil, A. S. Sergeenko, D. McKearney, S. Goeb, M. Sallé, D. B. Leznoff, T. Storr, *Chem. Commun.* **2019**, 55, 6082-6085.
73. Y. M. Jeon, J. Heo, C. A. Mirkin, *J. Am. Chem. Soc.* **2007**, 129, 7480-7481.
74. M. S. Masar, N. C. Gianneschi, C. G. Oliveri, C. L. Stern, S. T. Nguyen, C. A. Mirkin, *J. Am. Chem. Soc.* **2007**, 129, 10149-10158.
75. S. S. Sun, C. L. Stern, S. T. Nguyen, J. T. Hupp, *J. Am. Chem. Soc.* **2004**, 126, 6314-6326.
76. N. P. E. Barry, B. Therrien, *Eur. J. Inorg. Chem.* **2009**, 2009, 4695-4700.
77. H. Yan, G. Süss-Fink, A. Neels, H. Stoeckli-Evans, *J. Chem. Soc. Dalton Trans.* **1997**, 4345-4350.
78. R. E. Morris, R. E. Aird, S. Murdoch Pdel, H. Chen, J. Cummings, N. D. Hughes, S. Parsons, A. Parkin, G. Boyd, D. I. Jodrell, P. J. Sadler, *J. Med. Chem.* **2001**, 44, 3616-3621.
79. M. Ganeshpandian, R. Loganathan, E. Suresh, A. Riyasdeen, M. A. Akbarsha, M. Palaniandavar, *Dalton Trans.* **2014**, 43, 1203-1219.
80. M. M. Siddiqui, R. Saha, P. S. Mukherjee, *Inorg. Chem.* **2019**, 58, 4491-4499.
81. H. Lee, P. Elumalai, N. Singh, H. Kim, S. U. Lee, K. W. Chi, *J. Am. Chem. Soc.* **2015**, 137, 4674-4677.
82. Y. Cohen, L. Avram, L. Frish, *Angew. Chem. Int. Ed.* **2005**, 44, 520-554.
83. J. H. Jo, N. Singh, D. Kim, S. M. Cho, A. Mishra, H. Kim, S. C. Kang, K. W. Chi, *Inorg. Chem.* **2017**, 56, 8430-8438.
84. J. Singh, D. H. Kim, E. H. Kim, N. Singh, H. Kim, R. Hadiputra, J. Jung, K. W. Chi, *Chem. Commun.* **2019**, 55, 6866-6869.
85. L. Chiang, K. Herasymchuk, F. Thomas, T. Storr, *Inorg. Chem.* **2015**, 54, 5970-5980.
86. P. Singh, G. Mukherjee, A. K. Singh, *J. Organomet. Chem.* **2012**, 715, 33-38.
87. N. G. Connelly, W. E. Geiger, *Chem. Rev.* **1996**, 96, 877-910.
88. A. Kochem, G. Gellon, O. Jarjays, C. Philouze, A. du Moulinet d'Hardemare, M. van Gastel, F. Thomas, *Dalton Trans.* **2015**, 44, 12743-12756.
89. S. A. Odom, S. Ergun, P. P. Poudel, S. R. Parkin, *Energ. Environ. Sci.* **2014**, 7, 760-767.
90. S. Ghumaan, S. Mukherjee, S. Kar, D. Roy, S. M. Mobin, R. B. Sunoj, G. K. Lahiri, *Eur. J. Inorg. Chem.* **2006**, 2006, 4426-4441.
91. T. S. Kamatchi, S. Mondal, T. Scherer, M. Bubrin, K. Natarajan, W. Kaim, *Chem. Eur. J.* **2017**, 23, 17810-17816.
92. B. Sarkar, W. Kaim, J. Fiedler, C. Duboc, *J. Am. Chem. Soc.* **2004**, 126, 14706-14707.
93. M. Bubrin, D. Schweinfurth, F. Ehret, S. Zálíš, H. Kvapilová, J. Fiedler, Q. Zeng, F. Hartl, W. Kaim, *Organometallics* **2014**, 33, 4973-4985.
94. V. Vajpayee, Y. H. Song, Y. J. Jung, S. C. Kang, H. Kim, I. S. Kim, M. Wang, T. R. Cook, P. J. Stang, K. W. Chi, *Dalton Trans.* **2012**, 41, 3046-3052.
95. D. M. D'Alessandro, F. R. Keene, *Chem. Soc. Rev.* **2006**, 35, 424-440.
96. N. S. Hush, *Prog. Inorg. Chem.* **1967**, 8, 391-444.
97. N. S. Hush, *Coord. Chem. Rev.* **1985**, 64, 135-157.
98. L. Chiang, A. Kochem, O. Jarjays, T. J. Dunn, H. Vezin, M. Sakaguchi, T. Ogura, M. Orio, Y. Shimazaki, F. Thomas, T. Storr, *Chem. Eur. J.* **2012**, 18, 14117-14127.
99. Y. Shimazaki, T. D. P. Stack, T. Storr, *Inorg. Chem.* **2009**, 48, 8383-8392.
100. S. Grimme, J. Antony, S. Ehrlich, H. Krieg, *J. Chem. Phys.* **2010**, 132, 154104.
101. K. Arumugam, M. C. Shaw, J. T. Mague, E. Bill, S. Sproules, J. P. Donahue, *Inorg. Chem.* **2011**, 50, 2995-3002.

## TOC Graphic:



## TOC Text:

Self-assembly of redox-active Ni salen donors and Ru dimer acceptors affords a [2+2] rectangle for the shorter acceptor and a catenane for the longer acceptor. Catenane formation is dependent on solvent choice and concentration. Oxidation to form salen ligand radicals results in exciton coupling of the intense near-infrared intervalence charge transfer band confirming that the macrocycles remain intact upon oxidation.

## Keywords:

Self-assembly, macrocycles, redox-active ligands, oxidation, exciton coupling